magnetochemistry

MDPI

Article

Motion of Magnetic Microcapsules Through Capillaries in the Presence of a Magnetic Field: From a Mathematical Model to an In Vivo Experiment

Mikhail N. Zharkov [1,*], Mikhail A. Pyataev [1], Denis E. Yakobson [1], Valentin P. Ageev [1], Oleg A. Kulikov [1], Vasilisa I. Shlyapkina [1], Dmitry N. Khmelenin [2], Larisa A. Balykova [1], Gleb B. Sukhorukov [3] and Nikolay A. Pyataev [1,*]

[1] Federal Center for Biothechnology and Medicine Advancement, National Research Ogarev Mordovia State University (MRSU), Bolshevistskaya Str. 68, 430005 Saransk, Russia; pyataevma@gmail.com (M.A.P.); ykbsn@mail.ru (D.E.Y.); valeageev@yandex.ru (V.P.A.); oleg-kulikov-84@mail.ru (O.A.K.); shlyapkina.98@mail.ru (V.I.S.); larisabalykova@yandex.ru (L.A.B.)

[2] A.V. Shubnikov Institute of Crystallography, The Kurchatov Complex Crystallography and Photonics of the NRC "Kurchatov Institute" Sciences, 119991 Moscow, Russia; dirq@mail.ru

[3] Skolkovo Institute of Science and Technology, Bolshoy Boulevard 30, Bld. 1, 143025 Moscow, Russia; g.sukhorukov@skoltech.ru

* Correspondence: mikhail.zharkov.92@mail.ru (M.N.Z.); pyataevna@mail.ru (N.A.P.)

Abstract

In this paper, we discuss the prediction of the delivery efficiency of magnetic carriers based on their properties and field parameters. We developed a theory describing the behavior of magnetic capsules in the capillaries of living systems. A partial differential equation for the spatial distribution of magnetic capsules has been obtained. We propose to characterize the interaction between the magnetic field and the capsules using a single vector, which we call "specific magnetic force". To test our theory, we performed experiments on a model of a capillary bed and on a living organism with two types of magnetic capsules that differ in size and amount of magnetic material. The experimental results show that the distribution of the capsules in the field correlated with the theory, but there were fewer actually accumulated capsules than predicted by the theory. In the weaker fields, the difference was more significant than in stronger ones. We proposed an explanation for this phenomenon based on the assumption that a certain level of magnetic force is needed to keep the capsules close to the capillary wall. We also suggested a formula for the relationship between the probability of capsule precipitation and the magnetic force. We found the effective value of a specific magnetic force at which all the capsules attracted by the magnet reach the capillary wall. This value can be considered as the minimum level for the field at which it is, in principle, possible to achieve a significant magnetic control effect. We demonstrated that for each type of capsule, there is a specific radius of magnet for which the effective magnetic force is achieved at the largest possible distance from the magnet's surface. For the capsules examined in this study, the maximum distance where the effective field can be achieved does not exceed 1.5 cm. The results of the study contribute to our understanding of the behavior of magnetic particles in the capillaries of living organisms when exposed to a magnetic field.

Keywords: targeted drug delivery; polyelectrolyte capsules; magnetite nanoparticles; nanoparticle motion modeling

check for updates

Academic Editor: Carlos J. Gómez García

Received: 1 May 2025
Revised: 30 June 2025
Accepted: 8 July 2025
Published: 14 July 2025

Citation: Zharkov, M.N.; Pyataev, M.A.; Yakobson, D.E.; Ageev, V.P.; Kulikov, O.A.; Shlyapkina, V.I.; Khmelenin, D.N.; Balykova, L.A.; Sukhorukov, G.B.; Pyataev, N.A. Motion of Magnetic Microcapsules Through Capillaries in the Presence of a Magnetic Field: From a Mathematical Model to an In Vivo Experiment. *Magnetochemistry* **2025**, *11*, 60. https://doi.org/10.3390/magnetochemistry11070060

Copyright: © 2025 by the authors. Licensee MDPI, Basel, Switzerland. This article is an open access article distributed under the terms and conditions of the Creative Commons Attribution (CC BY) license (https://creativecommons.org/licenses/by/4.0/).

1. Introduction

One of the main challenges in the treatment of tumors and other localized diseases is the efficient delivery of medications to the site of pathology. With systemic administration, only a small proportion of the administered drug reaches the targeted site, while the majority is distributed throughout healthy tissues, causing various side and toxic effects. In light of this, methods for the targeted delivery of anticancer drugs are currently undergoing active development. Magnetic-driven drug delivery is an attractive approach due to the ability of magnetic fields to penetrate biological tissues. In recent years, various systems for magnetic drug delivery have been proposed, including those based on liposomes [1,2], micelles [3], inorganic nano- and microparticles [4–6], and polymer capsules [7]. The delivered substances can include antitumor [8], antibacterial [9], and anti-inflammatory drugs [10], nucleic acids [11], specific proteins [12], and others. The magnetic field can be used not only for drug delivery, but also for the movement of tissue spheroids [13], individual cells, and intracellular organelles loaded with magnetic particles [14,15].

One of the key challenges in this field is the development of magnetic systems with specific spatial configurations and field parameters required for the control and magnetic guidance of particles. Magnetic control of a single drop of ferrofluid in a Petri dish using four electromagnets was demonstrated in paper [16]. In the works [15,17], the so-called Halbach cylinders were used to construct magnetic guiding systems, allowing for contactless orientation and movement of magnetic objects. A comprehensive review on magnetic guiding systems based on permanent magnets can be found [18].

Despite this progress, in vivo magnetic targeting studies remain relatively rare compared to the number of in vitro experiments. Most investigations are performed on small animals. Almost all of these studies demonstrate the possibility of accumulation of systemically administered magnetic nanoparticles at the site of application of a permanent magnet: in the meninges [19], tumors [20], and limbs [21]. It is noted that the size and coating of the particles affect the efficiency of magnetic targeting [22,23].

There are also examples of research on magnetic drug targeting in large animals. A. Christoph et al. performed a study on rabbits with tumors, where they concentrated the 150 nm Fe_3O_4 nanoparticles conjugated with mitoxantrone, using the permanent magnet with a maximum induction of 0.4 T [24]. High-performance liquid chromatography demonstrated that magnetic targeting increases the concentration of mitoxantrone in the tumor by a factor of ten. H. Chen et al. studied the capture of micron-sized particles associated with a tissue plasminogen activator in the large arteries of macaques (*Macaca fascicularis*) [25]. Histological analysis confirmed the magnetic capture of these particles during intravenous and intra-arterial administration. In contrast, no particles were detected in arterial segments located away from the magnet or in the control limb.

Despite the large number of studies on magnetic targeted drug delivery, research on this topic rarely reaches the clinical stage. We found only one paper that reported a clinical trial of magnetic targeting for epirubicin coupled with 100 nm iron oxide nanoparticles [26].

Theoretical modeling and experimental investigation of the precipitation mechanism are essential for the proper selection of carrier parameters, such as particle size, magnetic content, magnetic field gradient, and others. At least a rough estimation of these parameters is necessary to assess the feasibility of magnetic targeting. A number of studies proposed approaches to such an assessment. For example, S. Sharma and P. Ram proposed a dimensionless parameter called the particle magnetization number, which allows for estimating the probability of particle capture in the magnetic field [27]. A. Nacev proposed three dimensionless parameters, one of which is the ratio of the magnetic force to the Stokes force, and the other two include the diffusion coefficients in the liquid and in the capillary wall [28]. The introduced parameters allow for predicting the behavior of the

system. Theoretical studies of the behavior of magnetic carriers in a fluid flow use two main approaches: analysis of particle trajectories [27,29–33] and solution of the partial differential equation for concentrations, following from the continuity equation for the flow [28,34,35]. It is worth noting that most theoretical studies do not include a comparison of theoretical calculations with experiments. Only a few studies compare the results of numerical solutions of the continuity equation with experimental data obtained from in vitro vascular models [16,27–29], and even fewer compare the results of modeling and experimental data in vivo [28].

A crucial aspect of the development of a magnetic targeting system is predicting the outcome of the procedure based on available magnet and particle parameters. Despite the large number of theoretical studies and experiments conducted both in vitro and in vivo, a gap remains between the theory and both types of experiments. This gap is a significant issue, primarily because real in vivo conditions are nearly impossible to replicate in laboratory setups, and secondly, because quantitative analysis of experimental results is most valuable when it can be compared with theoretical predictions. In this study, we propose a theoretical model that enables the evaluation of targeting efficiency. We investigated, both theoretically and in vitro, the precipitation process and distribution of magnetic capsules within a capillary subjected to an inhomogeneous magnetic field. Furthermore, we investigated the capture of magnetic polymer capsules in large animals (mini pigs), allowing us to perform a detailed quantitative analysis of the distribution of the capsules in lung tissue under the influence of a magnetic field. This enabled us to compare theoretical predictions with in vivo experimental results.

2. Materials and Methods

2.1. Obtaining and Characterization of Magnetic Polyelectrolite Capsules Containing Fe_3O_4 Nanoparticles

Iron (III) chloride hexahydrate, iron (II) chloride tetrahydrate, citric acid, polystyrene sulfonate sodium (PSS, M~70 kDa), polyallylamine hydrochloride (PAH, M~50 kDa), sodium dextran sulfate (DexS, M~40 kDa), and doxorubicin hydrochloride (DOX) were purchased from Sigma-Aldrich (Taufkirchen, Germany); 25% ammonia solution, sodium chloride, sulfosalicylic acid, 37% hydrochloric acid solution, sodium carbonate, calcium chloride, glycerin, dimethyl sulfoxide, isopropanol, and methanol were obtained from Vecton (St. Petersburg, Russia). All chemicals were used without further purification. Deionized water produced with the water treatment system Milli-Q (Merck Millipore, Darmstadt, Germany) was used in all experimental stages.

The iron oxide nanoparticles were obtained using the co-precipitation method described in our previous work [36]. Weighed portions of $FeCl_2 \cdot 4H_2O$ (0.43 g) и $FeCl_3 \cdot 6H_2O$ (1.17 g) were dissolved in 40 mL of deionized water. Then, 2 mL of 25% ammonium hydroxide were quickly poured into the iron salt solution with vigorous stirring in an argon atmosphere. After 5 min, 2 mL of citric acid (0.3 g/mL) were added to the obtained Fe_3O_4 particles and stirring was continued for 90 min at room temperature. The resulting colloid of Fe_3O_4 nanoparticles was purified by dialysis in cellulose membranes with a pore size of 12–14 kDa (Orange Scientific, Braine-l'Alleud, Belgium) for 72 h. The purified colloid was centrifuged at 12,000 rpm for 15 min to remove large aggregates. The hydrodynamic diameter and ζ-potential of the resulting Fe_3O_4 nanoparticles were 12 ± 4 nm and -34 ± 3 mV, respectively.

Microcapsules were synthesized using the "layer by layer" method by sequential adsorption of oppositely charged polyelectrolytes (PAH and DexS) and iron oxide nanoparticles on spherical $CaCO_3$ particles [13,37]. Since it is difficult to determine Fe_3O_4 in biological samples (given the presence of intrinsic iron in blood and tissues), doxorubicin

was used as a fluorescent label for indirect determination of magnetite quantity and analysis of capsule distribution. In addition, DOX is a therapeutic drug that can be delivered to the target organ or tissue.

The synthesis method involved three steps: synthesis of cores (spherical calcium carbonate particles), loading of DOX into the cores, and formation of shells of polymers and magnetic nanoparticles.

At the first stage, spherical micron $CaCO_3$ particles were synthesized by an ion exchange reaction between $CaCl_2$ and Na_2CO_3 in an aqueous medium with the addition of PSS. Under stirring (400 rpm), 1 mL of an aqueous solution of PSS (10 mg/mL) was added to 1.5 mL of 0.3 M aqueous solution of Na_2CO_3, then 1.5 mL of 0.3 M aqueous solution of $CaCl_2$ was quickly added and the mixture was stirred for 1 min. The resulting spherical $CaCO_3$ microparticles were precipitated by centrifugation (1200 rpm, 1 min) and washed 3 times with deionized water. Submicron $CaCO_3$ particles were obtained similarly, but with the addition of glycerol as a particle growth stabilizer [21]. At the next stage, doxorubicin was loaded into $CaCO_3$@PSS particles by 5-h incubation of an aqueous solution of the drug with nuclei at a temperature of 10 °C. To submicron or micron $CaCO_3$ particles obtained from one synthesis and dispersed in 1 mL of deionized water, 1 mL of doxorubicin hydrochloride (0.2 mg/mL) was added. The particles with DOX were incubated for 1 h and then washed 3 times with deionized water to remove free drugs.

The capsule shells were formed from positively charged PAH and negatively charged DexS and iron oxide nanoparticles. Polymer solutions with a concentration of 2 mg/mL were prepared in 0.5 M NaCl solution. PAH (1 mL of an aqueous solution) was added to the core suspension and vigorously mixed on a shaker at 1600 rpm for 15 min. After that, the core suspension with the first layer of positively charged polyelectrolyte was centrifuged and washed three times with deionized water. To prevent particle aggregation, the suspension was subjected to short-term (5 s) ultrasound treatment (35 kHz, 100 W). Negatively charged DexS was applied as the next layer using the same technique. The process of application and washing was similarly repeated for subsequent capsule layers. Magnetic Fe_3O_4 nanoparticles, having a negative charge, were applied to a layer of positively charged PAH polyelectrolyte. Then, 1 mL of a suspension of Fe_3O_4 nanoparticles with a concentration of 0.5 mg/mL was added to $CaCO_3$ particles coated with an outer layer of PAH and the mixture was vortexed for 15 min. After all layers had been applied, the capsules were washed several times with deionized water and dispersed in a 0.9% NaCl solution. Finally, to remove large aggregates, the resulting capsule suspensions were passed through a metal filter with a pore size of 1 and 5 μm (for submicron and micron capsules, respectively). Thus, we obtained capsules containing a core consisting of calcium carbonate and polystyrene sulfonate with adsorbed doxorubicin. The shell was represented with several layers of oppositely charged polymers (PAH and PSS) and iron nanoparticles incorporated between them. The capsules can be described by the following formula: $CaCO_3$@PSS-DOX/$(PAH/NpFe_3O_4)_3$/$(PAH/DexS)_2$.

The morphological characteristics of the obtained magnetic capsules were assessed using the transmission electron microscopy (TEM) (Tecnai Osiris microscope, FEI Company, Hillsboro, OR, USA) with a SuperX EDS system for ultrafast elemental mapping). The ζ-potential was measured using a Stabino analyzer (Microtrac Inc., Krefeld, Germany). The amount of iron in the capsules and Fe_3O_4 colloid was determined using a photocolorimetric method based on measuring the optical density of yellow-colored complexes of iron (III) ions with sulfosalicylic acid in an alkaline medium [38]. The content of DOX in capsule suspensions was determined by a modified fluorimetric method [39,40] described in the Supplementary Materials (Section S1). The magnetization of capsule suspensions was

measured using an EZ11 vibration magnetometer (Microsense Inc., Lowell, MA, USA) at room temperature (≈25 °C).

2.2. In Vivo Experiment

All experiments on animals were treated according to the rules of the University Ethics Committee at MRSU (protocol No. 119 dated 15 September 2023) and the Geneva Convention of 1985 (International Guiding Principles for Biomedical Research Involving Animals). Mature mini pigs, aged 6 months and weighing 12–14 kg, were obtained from Svetlogorsk breeding center. The use of smaller animals was impossible due to the fact that it is impossible to adequately assess the field gradients for them and obtain pieces of organs sufficient for a correct assessment of biodistribution. The experiment was carried out with the use of intravenous anesthesia with muscle relaxation and mechanical lung ventilation. Zoletil (Zolazepam, Virbac Sante Animale Company, Carros, France) at a dose of 15 mg/(kg·h) and Rometar (Xylazine hydrochloride, Bioveta Company, Ivanovice na Hane, Czech Republic) at a dose of 1.5 mg/(kg·h) were used for anesthesia and rocuronium was used for muscle relaxation (1 mg/kg after induction and followed by infusion of either 2.5 mg/kg/h).

A total of six mini pigs were used, which were divided into two groups of three animals per group. Animals in the first group were given micron capsules, while those in the second group were given submicron capsules. The dose of magnetite was 0.65 mg/kg for both groups of animals.

Left thoracotomy was performed. A permanent cylindrical magnet (the same which was used for the in vitro experiments) was placed into the pleural cavity along the left posterior lateral line in such a way that the axis of the magnet passed through the middle of the caudal lobe of the left lung. To prevent the magnet from moving, a second magnet was installed on the outside of the chest. After fixing the magnets, the suspension of capsules was injected into the ear vein. One hour after administration of the capsules, euthanasia was performed by intravenous administration of 10 mL of 10% potassium chloride.

The heart–lung complex was taken out (the left and right caudal lobes were separated without allowing them to collapse) and placed in a freezer at −25 °C. After freezing, a cylindrical core with a diameter of 15 mm was cut out from a part of the lung located under the magnet so that the axis of the core coincided with the axis of the magnet. Then, the core was sliced into 3 mm-thick pieces. The mass of the entire piece and the mass of the magnetite it contained were determined (the method is described in the Supplementary Materials (Section S1)). Then, based on the assumption that the blood flowing through the lung was evenly distributed, the total amount of magnetite that passed through the piece was determined.

3. Results

3.1. Theoretical Model

The theoretical model is based on the analysis of capsule motion in a liquid, taking the diffusion into account. Here, we use a formulation based on a partial differential equation for the capsule concentration utilized previously in [28,34], since it provides a more convenient framework for quantitative comparison with experimental data. In this approach, the concentration of capsules n and the vector of capsules flux $\vec{j}$ satisfy the continuity equation:

$$\frac{\partial n}{\partial t} + \nabla \vec{j} = 0. \quad (1)$$

To take the diffusion into account, we consider the expression for microcapsule flux, including the drift and diffusive terms in it:

$$\vec{j} = n\vec{v} - D\nabla n, \tag{2}$$

where $\vec{v}$ is the drift velocity of the capsule in the capillary, and D is the diffusion coefficient. For a pure liquid, coefficient D can be determined based on the Stokes–Einstein equation for diffusion of a spherical particle through a viscous fluid:

$$D = \frac{kT}{6\pi\eta r}, \tag{3}$$

where k is the Boltzmann constant, T is temperature, η is the dynamic viscosity of the liquid, and r is the radius of capsule.

In the stationary regime, n is independent of time, and we obtain from Equations (1) and (2) the following:

$$\vec{v}\nabla n + n\nabla\vec{v} - D\Delta n = 0, \tag{4}$$

where Δ is the Laplace operator.

The total capsule drift velocity can be represented in the form of the following equation:

$$\vec{v} = \vec{v}_l + \vec{v}_r\,, \tag{5}$$

where $\vec{v}_l$ is the liquid velocity and $\vec{v}_r$ is the relative velocity of the capsule with respect to the liquid.

We assume that the capsules do not disturb the flow of liquid due to their low concentration. Consequently, the liquid velocities in the capillary follow Poiseuille's theory:

$$\vec{v}_l(\rho) = \vec{v}_0\left(1 - \frac{\rho^2}{R^2}\right), \tag{6}$$

where ρ is the distance from the capillary axis, R is the capillary radius, and $\vec{v}_0$ is the velocity of the liquid at the capillary axis.

The forces acting on the capsule are shown schematically in Figure 1. To find the relative velocity $\vec{v}_r$, we consider the Newton's law of motion for the microcapsule:

$$m\vec{a} = m\vec{g} + \vec{F}_m + \vec{F}_d + \vec{F}_b, \tag{7}$$

where $\vec{g}$ is the standard gravity, m is the mass of the capsule, $\vec{a}$ is its acceleration, $\vec{F}_d$ is the Stockes drag force, $\vec{F}_b$ is the buoyant force, and $\vec{F}_m$ is the magnetic force.

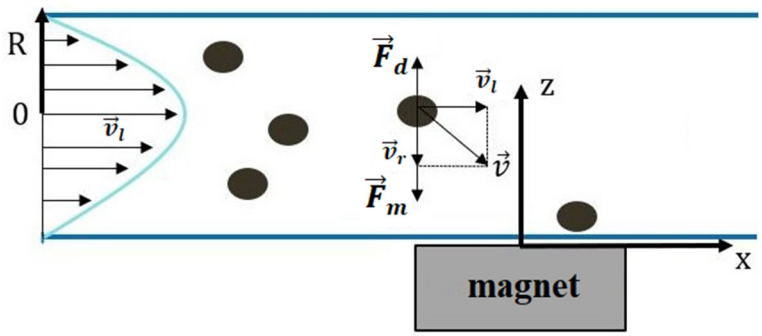


Figure 1. Schematic representation of a capsules moving in a capillary and the main forces acting on them (magnetic and drag force).

Because of the very small radius of the particle, all forces proportional to r^3, except $\vec{F}_m$, are much smaller than the drag force. Therefore, we can ignore inertia $m\vec{a}$, gravity, and buoyancy. Therefore, the equation of motion becomes the following:

$$\vec{F}_d + \vec{F}_m = 0. \tag{8}$$

The magnetic force acting on the particles can be found from the following equation:

$$\vec{F}_m = \left(\vec{p}_m \nabla\right)\vec{B}, \tag{9}$$

where $\vec{p}_m$ is the capsule average magnetic moment that is calculated based on experimentally measured magnetization of the suspension. The moment $\vec{p}_m$ is proportional to the mass m_{mag} of magnetite incorporated in the capsule:

$$\vec{p}_m = m_{mag}\vec{\sigma}, \tag{10}$$

where $\vec{\sigma}\left(\vec{B}\right)$ is the specific magnetization or the magnetic moment per unit of magnetite mass. Since the capsules are in a liquid medium, they can rotate, and their average magnetic moment is always directed parallel to $\vec{B}$. Consequently, specific magnetization can be represented in the following form:

$$\vec{\sigma}(\vec{B}) = \chi(B)\vec{B}, \tag{11}$$

where $\chi(B)$ is the specific magnetic susceptibility.

Magnetic field $\vec{B}$ and components of its gradient have been calculated for every point of space using the model of a homogeneously magnetized cylinder. Since the magnetic force is directly proportional to the mass of magnetite m_{mag} in the capsule, it is useful to represent it in the following form:

$$\vec{F}_m = m_{mag}\vec{f}_m. \tag{12}$$

Here, we introduced a new parameter $\vec{f}_m$ with the dimension of acceleration, which we call the specific magnetic force. It is defined by the following equation:

$$\vec{f}_m = \chi(B)(\vec{B}\nabla)\vec{B}, \tag{13}$$

and characterizes the interaction between the capsule and the magnetic field by a single vector. The value of $\vec{f}_m$ is almost independent of the capsule size and properties of liquid. Actually, it depends on the shape of the magnetization curve $\sigma(B)$, but the curves are quite similar for different types of capsules. It is worth noting that the value of $\vec{f}_m$ can be calculated in advance before solving the equation for the capsule's motion.

The distribution of a specific magnetic force in the axial plane for the magnet used in our experiments is shown in Figure 2. Magnetic field was calculated using the "magnetic charge" approach described in [41]. The exact equations corresponding to this approach for the magnetic field of a homogeneous longitudinally magnetized cylindrical magnet can be found in [42]. One can see in the figure that at small distances from the magnet, the values of f_m reach its maximal value near the edges of the cylinder base. However, at larger distances, the maximal value of f_m is located at the axis of the magnet.

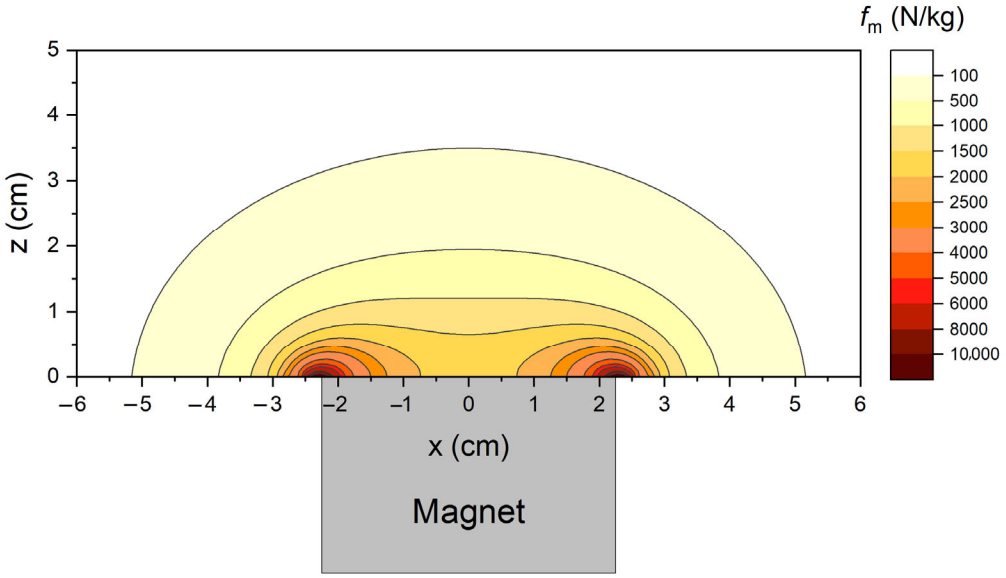


Figure 2. Specific magnetic force in the axial plain of the magnet.

We note that the specific magnetic force necessary for the targeted drug delivery is to be at least two orders of magnitude higher than the standard gravity g. Otherwise, the magnetic field will only be able to affect very large capsules, which could become uncontrollably precipitated in the normal gravitational field.

Let us consider now the drag force $\vec{F}_d$ in Equation (8). It is proportional to the relative velocity $\vec{v}_r$ and can be determined by the Stokes formula for spherical particle of radius r:

$$\vec{F}_d = -6\pi\eta r\vec{v}_r. \tag{14}$$

Then, from Equations (8), (12) and (14) we can find $\vec{v}_r$ and represent the total capsule velocity in the form of

$$\vec{v} = \vec{v}_l + \frac{m_{mag}}{6\pi\eta r}\vec{f}_m. \tag{15}$$

We note that the equivalent equation was used previously in [27,31,34]. Taking into account that $\nabla\vec{v}_l = 0$, we finally obtain the following from Equations (4) and (15):

$$\left(\vec{v}_l + \frac{m_{mag}}{6\pi\eta r}\vec{f}_m\right)\nabla n + n\frac{m_{mag}}{6\pi\eta r}\nabla\vec{f}_m - D\Delta n = 0. \tag{16}$$

Equation (16) allows us to find the concentration and flow rate of capsules in every point of the capillary. We note that the values of $\vec{f}_m$ are calculated in advance before solving Equation (16).

The value of concentration n is calculated numerically from Equation (16), which is solved in the cylindrical area of the capillary defined by inequalities

$$x_{min} < x < x_{max} \tag{17}$$

and

$$y^2 + z^2 < R^2, \tag{18}$$

where x_{min} and x_{max} are chosen to be far enough from the magnet. The boundary conditions are taken in the Cauchy form at half the cylindrical surface, i.e., both the concentration and velocity of particles are fixed on the left base ($x = x_{min}$) and on the upper part of the lateral

surface ($z > 0$) of the cylinder. The boundary conditions on the right base ($x = x_{max}$) and on the bottom of the cylinder ($z < 0$) remain unspecified.

The partial differential Equation (16) was solved with the grid method using the Scilab 6.1.1 software. The concentration of particles in the initial flow is taken to be homogenous. The flux of capsules was found by Equation (2), with the values of concentration obtained from the solution of Equation (16).

An example of capsule distribution in the axial cross-section of the capillary is shown in Figure 3.

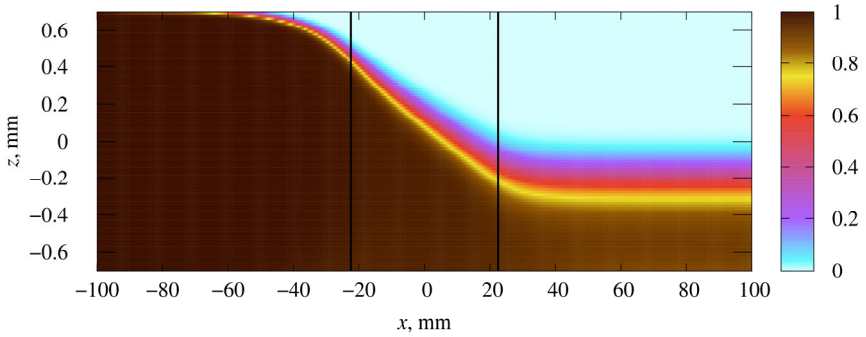


Figure 3. Calculated concentration distribution of submicron capsules in an axial section of a capillary with PBS. The distance between the capillary and the magnet is 13 mm.

As can be seen in the figure, the magnetic field causes the magnetic carriers to shift in the direction perpendicular to the flow. When the capillary is closer to the magnet, almost all particles are attracted by the field and the flow of liquid becomes purified. However, at larger distances, the proportion of settled particles decreases.

In this model, all the capsules reaching the bottom of the capillary are assumed to precipitate. In this assumption, the percentage of precipitated particles in the stationary regime is proportional to the particle vertical flux at the bottom of the cylinder. Integrating the flux over the y-coordinate and dividing it by the initial flux, we obtain the relative one-dimensional density $\rho(x)$ of precipitated capsules:

$$\rho(x) = \frac{1}{q}\int_{-r}^{r} j_z(x, y, z(y))dy, \tag{19}$$

where q is the total initial flux defined by the following equation:

$$q = \int j_x(x_{min}, y, z)dydz. \tag{20}$$

The function $\rho(x)$ is normalized so that the area under curve (AUC) defines the total fraction P of precipitated capsules:

$$P = \int_{x_{min}}^{x_{max}} \rho(x)dx. \tag{21}$$

The value of P can be considered as the total probability of capsule precipitation within the model used here.

3.2. Magnetite Containing Capsules

To test the developed theory and study experimentally the behavior of magnetic particles in a liquid flow, polyelectrolyte capsules containing magnetic iron oxide nanoparticles and doxorubicin were synthesized.

The results of the morphology study of polyelectrolyte magnetic capsules using TEM are shown in Figure 4 (bright-field images and element distribution maps).

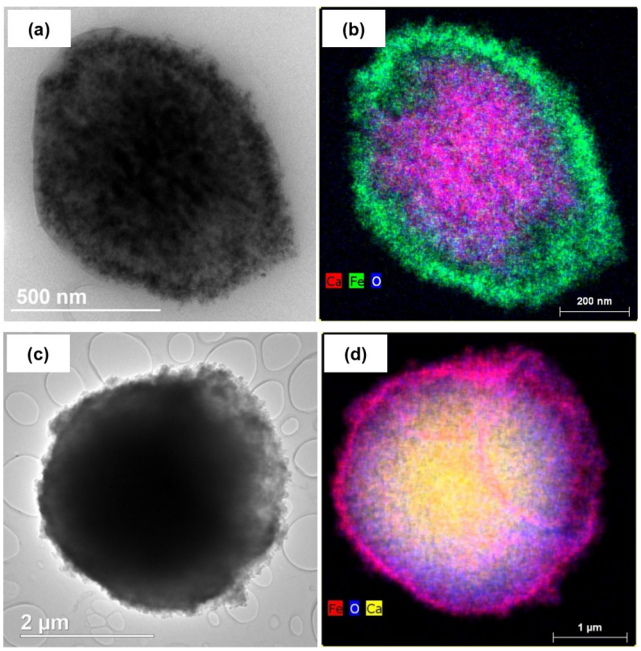


Figure 4. TEM images of a submicron (**a**,**b**) and micron (**c**,**d**) capsule containing magnetic iron oxide nanoparticles. Bright-field images (**a**,**c**) and chemical elements (Fe, Ca, and O) mapping (**b**,**d**).

As seen in Figure 4, the polymer capsules have a rounded shape and the iron oxide nanoparticles are uniformly distributed on the capsule shell. The average diameters were 820 ± 80 nm for submicron capsules and 2.5 ± 0.5 μm for micron capsules. Analysis of element distribution maps has shown that the capsules contain $CaCO_3$ cores and iron oxide nanoparticles in the polymeric shell. The electrokinetic potential is -14 ± 1 mV and -19 ± 2 mV for submicron and micron capsules (in 0.9% NaCl solution, pH = 7.4), respectively. The average magnetite content per capsule was $0.65 \cdot 10^{-12}$ g and $1.5 \cdot 10^{-12}$ g for submicron and micron capsules, respectively.

The magnetization curves of suspensions of the capsules are shown in Figure 5.

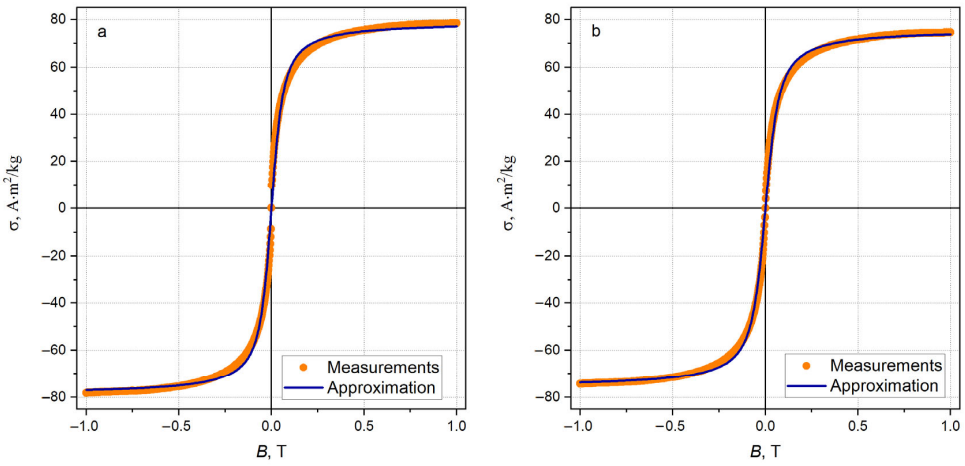


Figure 5. The specific magnetization of submicron capsules (**a**) and microcapsules (**b**) as a function of an external magnetic field (orange dots). Blue lines correspond to Langevin function approximation with parameter B_c = 0.025 T for submicron capsules and B_c = 0.029 T for micron ones. The specific saturation magnetization σ_s is equal to 79 $A \cdot m^2/kg$ and 76 $A \cdot m^2/kg$ for submicron capsules and microcapsules, respectively.

The magnetization curves are well approximated by the Langevin function:

$$\sigma(B) = \sigma_s L\left(\frac{B}{B_c}\right), \tag{22}$$

where σ_s is specific saturation magnetization, B_c is characteristic magnetic field, and $L(x)$ is the Langevin's function, which is given by the following equation:

$$L(x) = \coth(x) - \frac{1}{x}. \tag{23}$$

3.3. In Vitro Experiment

To evaluate the developed theory, an experimental setup was created to investigate capsule precipitation in a blood vessel. A model of a blood capillary was created using a polyethylene tube with an inner diameter of 1.4 mm. A schematic representation of the device is shown in Figure 6.

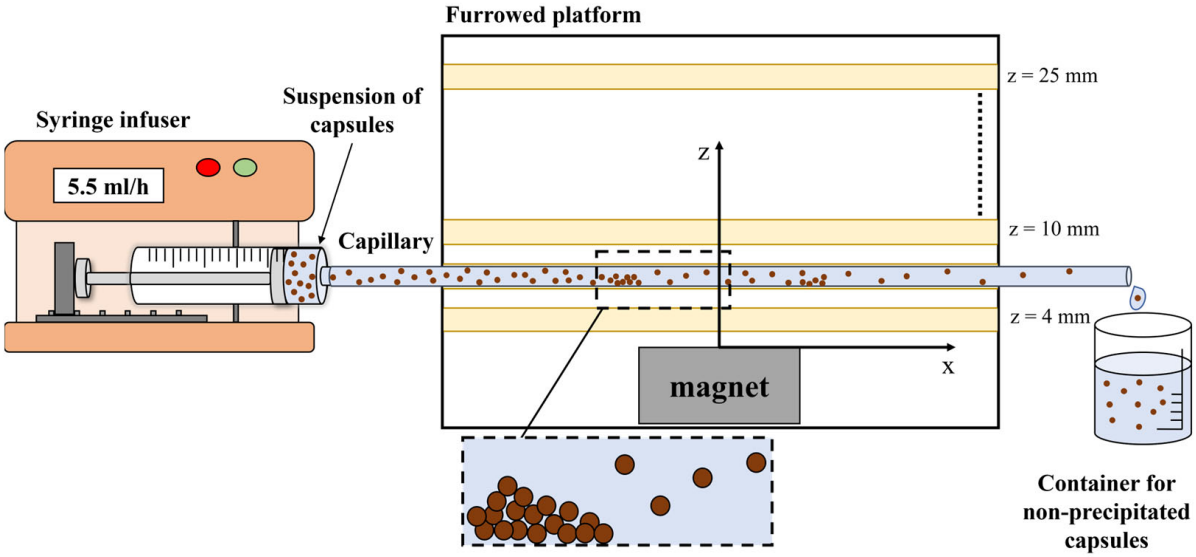


Figure 6. Scheme of the device for the in vitro experiment.

The capillary is located near the permanent NdFeB magnet of cylindrical shape. The magnet has a diameter of 45 mm and a height of 30 mm. The magnetization vector is parallel to the z-axis of the cylinder. The suspension of capsules was pumped through the capillary by the syringe infuser, allowing precise control of the flow rate.

Before pumping through the capillary, the capsules were resuspended in phosphate buffered saline (PBS) or blood. To study the spatial distribution of precipitated capsules in the magnetic field, the capillary was fixed at the distance z from the magnet base and then 2 mL of suspension were pumped through it at a flow rate of 20 mL/h. After that, the flow was stopped, and the capillary was frozen and then cut in pieces of 5 mm in length. The content of the capsules in each piece was determined by the amount of doxorubicin, which was measured by modified fluorimetric method [39,40]. A detailed description of the fluorimetric method for quantitative analysis of doxorubicin is given in the Supplementary Materials (Section S1).

The results of the calculations and experimental measurements of the precipitated capsule concentration in the capillary in PBS medium are shown in Figure 7.

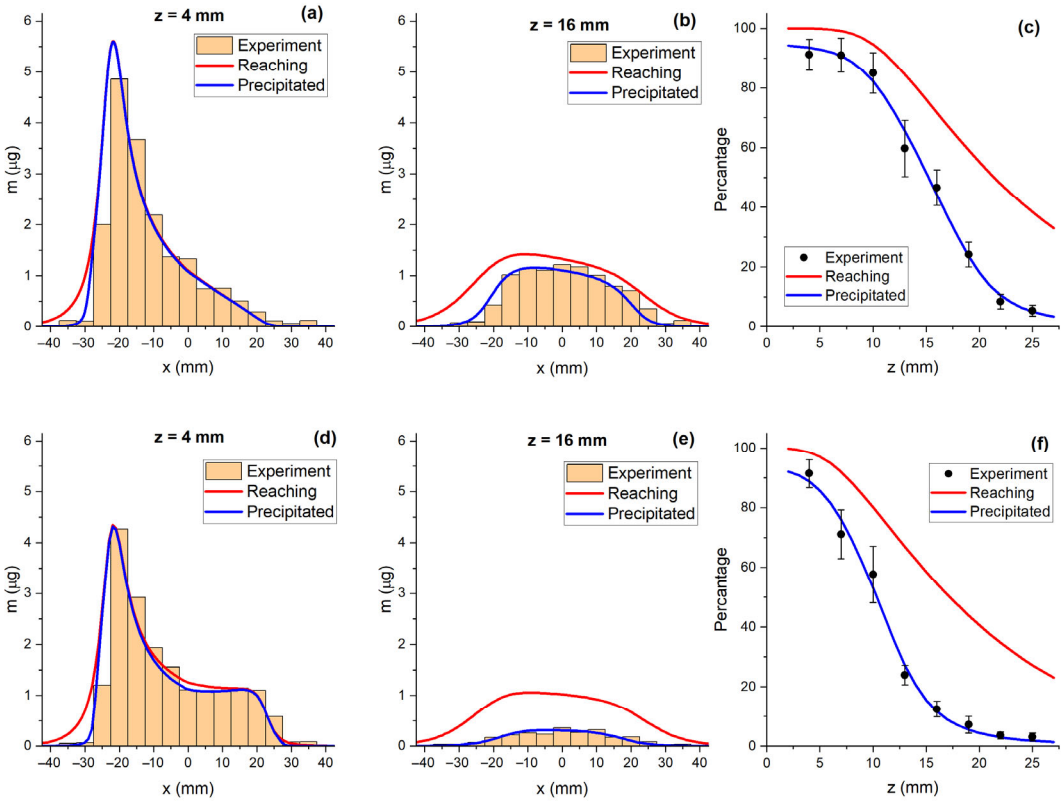


Figure 7. Distribution of deposited capsules in a model capillary with PBS. (**a**–**c**) correspond to submicron capsules and (**d**–**f**) show the distribution of microcapsules. (**a**,**b**,**d**,**e**) show the amount of magnetite contained in precipitated capsules as a function of longitudinal coordinate x in the capillary. The columns represent the experimentally measured amount of magnetite in the capillary pieces, the red curve corresponds to the calculated number of capsules reaching the capillary wall, and the blue curve represents the number of settled capsules calculated using function (24). (**a**,**d**) show the distributions for the distance z = 4 mm between the capillary and the magnet, while (**b**,**e**) correspond to z = 16 mm. In (**c**,**f**), the dots show the experimentally measured percentage of capsules deposited along the entire length of the capillary at various distances z from the capillary to the magnet, the red line shows the percentage of capsules reaching the wall, and the blue line shows the percentage of settled capsules calculated using function (24).

The experimentally determined amount of magnetite deposited in the capillary depending on the longitudinal coordinate is represented by the columns in Figure 7a,b,d,e. It can be seen that at small distances z between the capillary and the magnet, the largest number of particles are deposited near the edges of the magnet, where the magnetic force is at its maximum. At larger distances between the capillary and magnet, the maximum force is located close to the magnet axis and the maximum of capsules concentration is also observed there. In Figure 7c,f, the dots show the dependence of the percentage of capsules deposited along the entire length of the capillary on the distance to the magnet. The red solid line in these figures represents the theoretically calculated percentage of capsules that reach the capillary wall. It can be seen that the initial section of the red curve in Figure 7c (up to approximately 8 mm) is horizontal. This range of distances corresponds to magnetic fields at which all capsules reach the capillary wall during their movement along the magnet.

As can be seen in Figure 7c,f, the number of precipitated capsules measured experimentally is significantly lower than the number that reach the wall. To explain this difference, we propose that capsules that reach the wall continue to experience a pulling force from the liquid. In many cases, they do not stop but continue to move along the wall. If the

size of the capsules was negligible, they would remain in the region of the liquid with zero velocity after reaching the capillary wall. However, since their size is finite, even after touching the wall, they remain in a region of liquid with non-zero flow velocity.

One of the simplest models that can describe the detachment of capsules from the capillary wall is the dry friction model. According to this model, to carry the capsule away, the Stokes force must overcome the static friction force proportional to the normal force. In the considered case, the normal force is caused by the magnetic attraction. In the dry friction model, there is a threshold specific magnetic force f_0, starting from which the particle remains settled, while at lower values of f_m, it is carried away by the flow. Thus, the dependence of the probability of particle sedimentation on magnetic force will be described by the Heaviside step function.

However, in real systems, there are many factors that make the step function appear smooth. We can mention, for example, dispersion of capsule sizes and adhesive properties, inhomogeneity of the capillary wall, formation of conglomerates of precipitated capsules, irregularity of liquid velocity distribution, etc. A smooth step-like function can be created in an infinite number of ways, and each of these functions can have a number of parameters, allowing one to achieve a fairly good approximation of the experimental data. One of the simplest functions of this type is, for example, the following:

$$\alpha(u) = \frac{1}{2}\left(1 + \frac{u}{\sqrt{1+u^2}}\right), \tag{24}$$

where the argument u has the form

$$u = \frac{f - f_0}{\Delta f}. \tag{25}$$

The parameter f_0 determines the magnitude of a specific magnetic force at which half of the capsules reaching the capillary wall are precipitated. The parameter Δf is responsible for the broadening of the function. Its value depends on the chosen formula for the smoothed Heaviside function.

The blue lines in Figure 7 show the dependence of the percentage of settled capsules, obtained by multiplying the percentage of capsules that reached the wall by the probability of their precipitation, calculated by Formula (24). The parameters f_0 and Δf were obtained from the best coincidence between the theoretical calculation and experimental measurement for the total amount of precipitated capsules. The values of the parameters were $f_0 = 600$ m/s^2 and $\Delta f = 260$ m/s^2 for submicron capsules, and $f_0 = 940$ m/s^2 and $\Delta f = 380$ m/s^2 for micron ones.

As can be seen in Figure 7a,b,d,e, there are regions where the blue line is significantly lower than the red one. According to our theory, this indicates that in these areas, the capsules reach the capillary wall, but the magnetic force is not strong enough to keep them in place, and most of them are carried away by the flow. This effect is especially noticeable at distances greater than 12 mm for submicron capsules, and greater than 7 mm for micron-sized ones.

In addition to the experiments with PBS, we also studied particle motion in blood diluted in equal parts with normal saline. The results of the experiments with blood are presented in Figure 8. As can be seen in the figure, the number of precipitated capsules of both types in blood is significantly lower than in PBS. The presence of blood cells leads to an increase in overall viscosity, which results in an increased magnetic force required to bring the capsules to the capillary walls, as well as an increased force needed to keep them near the walls. The calculated parameters of function (24) used for the estimation of the number of precipitated capsules in the case of blood were $f_0 = 1720$ m/s^2 and $\Delta f = 910$ m/s^2 for

submicron capsules and $f_0 = 2330$ m/s^2 and $\Delta f = 1440$ m/s^2 for micron ones. We note that the value of the parameter f_0 is about three times larger for blood than for PSB for both types of capsules. This means that the force required to keep the capsule near the capillary wall is greater in the case of blood.

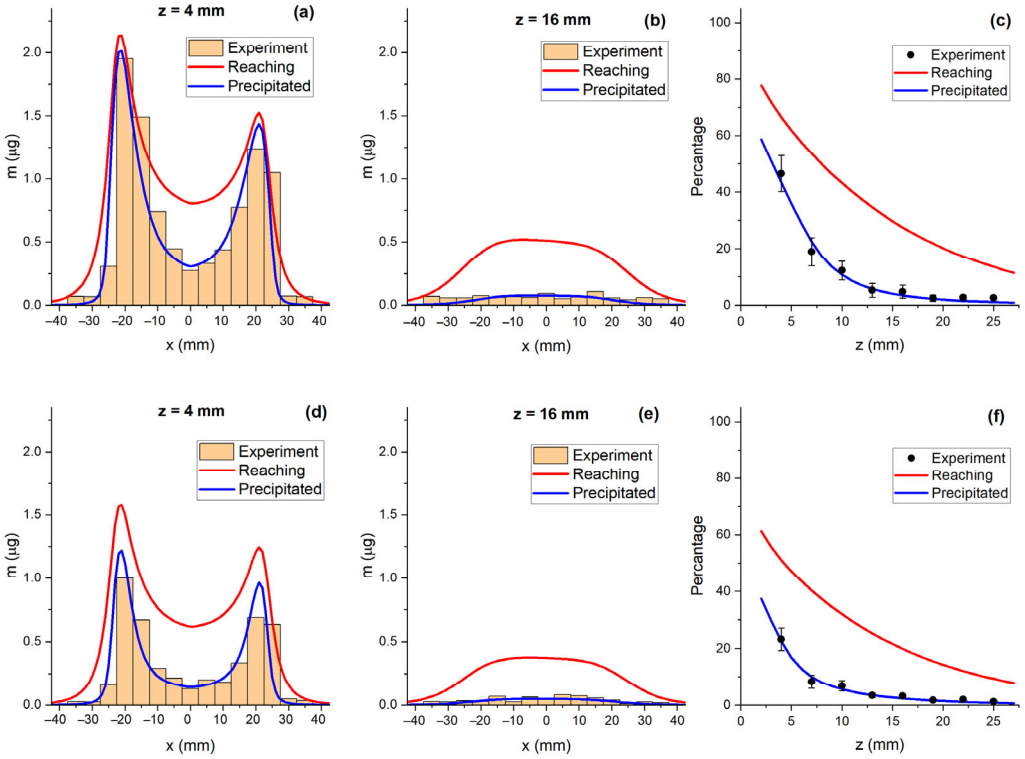


Figure 8. Distribution of deposited capsules in a model capillary with diluted blood. (**a**–**c**) correspond to submicron capsules and (**d**–**f**) show the distribution of microcapsules. (**a**,**b**,**d**,**e**) show the amount of magnetite as a function of longitudinal coordinate x in the capillary. The columns represent the experimentally measured amount of magnetite in the capillary pieces, the red curve corresponds to the calculated number of capsules reaching the capillary wall and the blue curve represents the number of settled capsules calculated using function (24). (**a**,**d**) show the distributions for the distance z = 4 mm between the capillary and the magnet, while (**b**,**e**) correspond to z = 16 mm. In (**c**,**f**), the dots show the experimentally measured percentage of capsules deposited along the entire length of the capillary at various distances z from the capillary to the magnet, the red line shows the percentage of capsules reaching the wall, and the blue line shows the percentage of settled capsules calculated using function (24).

As can be seen in Figure 8a,d, there is a second peak in the dependence of capsule concentration on coordinate x in the region near the far edge of the magnet. This peak is due to the presence of two maxima in the magnetic force near the edges of the magnet. Unlike the case of PBS, where almost all the capsules precipitate near the first edge of the magnet, the high viscosity of the blood leads to the appearance of the capsules which do not have enough time to precipitate when passing the first region of the maximum field. However, their position in the capillary becomes much closer to the magnet, and when the capsules pass the second peak of the field, most of them reach the capillary wall.

Within the framework of our theory, capsules that reach the capillary wall in areas with strong magnetic force remain settled, as the friction force between the capsule and the wall is strong enough to keep them in place. However, for capsules that reach the wall in regions with a lower magnetic field, the attractive force may be insufficient for settling the capsules, and there is a significant chance that they will be swept away from the wall and continue to move. This explains the fact that the blue and red theoretical curves practically

coincide in the region of strong fields and differ noticeably in the region of lower magnetic force, in particular, in Figure 8b,e and near $x = 0$ in Figure 8d.

As can be seen in Figure 8f, the curve representing the number of microcapsules that reach the capillary wall does not have an initial horizontal section. This indicates that in the case of more viscous liquids, the magnetic field is insufficient to move all of the capsules in the flow towards the capillary wall. Additionally, the percentage of precipitated capsules may decrease in this scenario because a greater force would be required to keep them near the wall.

3.4. In Vivo Experiment

The in vivo experimental design is shown in Figure 9 and described in detail in the Materials and Methods section. In brief, we determined the concentration of magnetite in the mini pig's lungs to which a permanent magnet was placed. The concentration of magnetite was measured at several distances from the magnet limited by the pig's lung size.

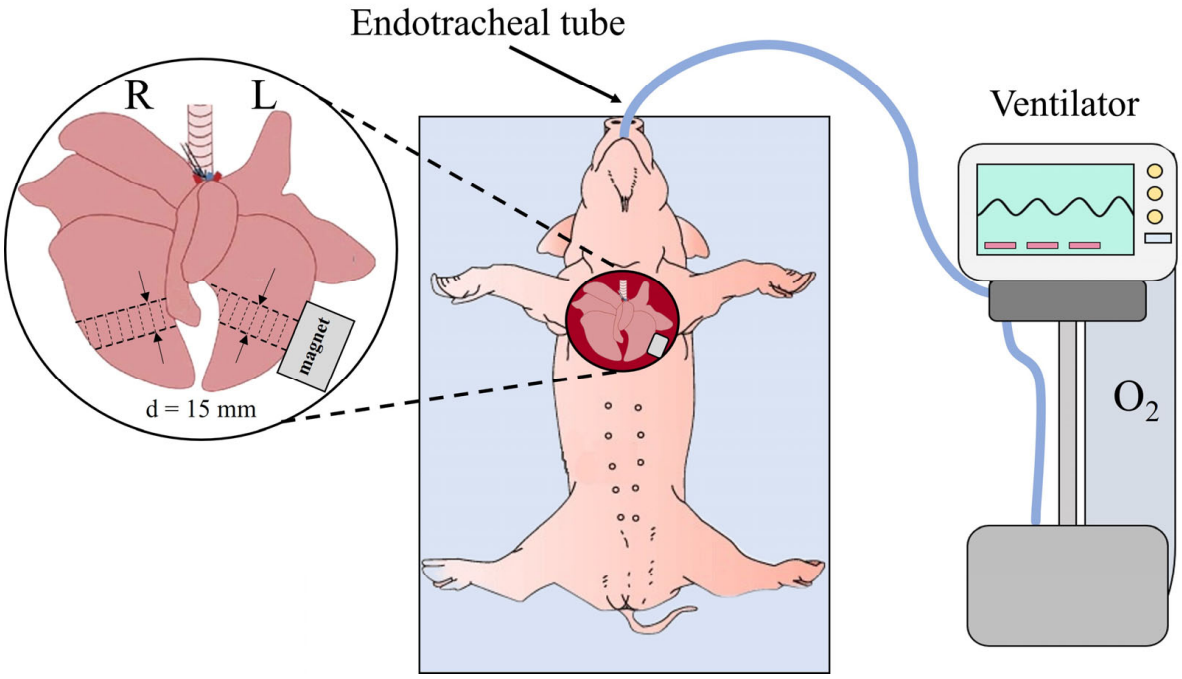


Figure 9. Schematic representation of the in vivo experiment in mini pigs. The left thoracotomy was performed along with intravenous anesthesia and mechanical ventilation. A cylindrical permanent magnet was placed close to the surface of the lower lobe of the left lung. Then, a suspension of submicron or micron capsules was introduced into the ear vein, and magnetite dose was equal for both type of capsules. After euthanasia, the lungs were removed and the concentration of magnetite in the lung tissue under the magnet and in the opposite lung (without a magnet) was determined.

The following model was used to calculate the number of capsules deposited in the lung tissue of a mini pig: A straight cylindrical capillary with a diameter of $D = 15$ μm and a length of $l = 600$ μm was considered [43]. The average blood flow velocity was chosen to be $\overline{v} = 1$ mm/s, and the blood viscosity was $\eta = 5$ mPa · s [44]. Due to the small size of the capillary, the magnetic force inside it was considered to be uniform. To simplify the calculations, it was also considered that the magnetic force was the same at all points of the selected piece of lung.

It was taken into account that the angle θ between the capillary and the direction of the magnetic force can take arbitrary values. The calculation of the number of capsules reaching the wall for different values of the angle θ was carried out by numerically solving

Equation (16). Then, the percentage of capsules reaching the wall was averaged in all possible directions of the capillary using the formula

$$\langle f \rangle = \frac{1}{2}\int_0^{\pi} f(\theta) sin\theta d\theta. \quad (26)$$

The integral was found numerically by the trapezoid method.

The results of the study of the micron and submicron magnetic capsule biodistribution are shown in Figure 10.

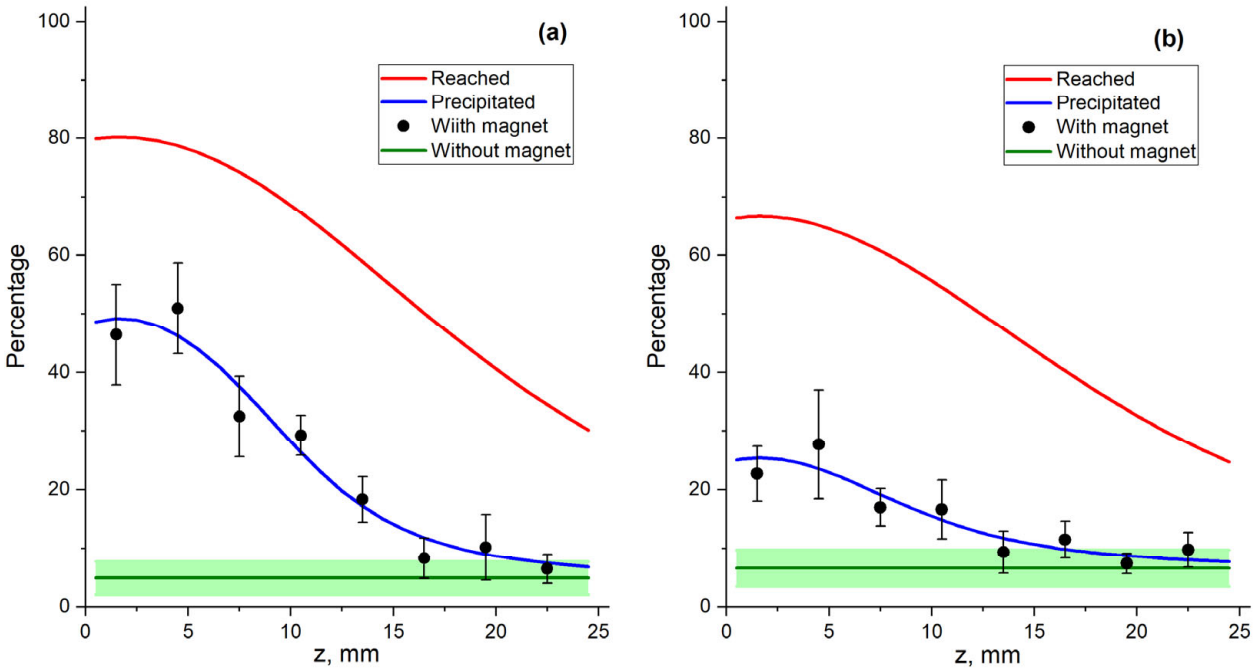


Figure 10. Percentage of submicron (**a**) and micron (**b**) capsules accumulated in the lung tissue under the influence of the magnetic field as a function of distance z from the magnet. Points represent the results of experimental measurements; the red line is the calculated percentage of capsules reaching the wall of the capillary and the blue one corresponds to is the percentage of precipitated capsules calculated with Equation (24).

Here, the black dots represent the experimentally determined amount of magnetite in a lung piece as a percentage of the total amount of magnetite passing through the piece. The red curve shows the theoretically calculated percentage of capsules reaching the capillary wall. The blue curve is a theoretical estimation of the percentage of precipitated capsules. It is obtained by multiplying the number of capsules reaching the capillary wall by function (24). The parameters f_0 and Δf of function (24) are selected in such a way that the resulting curve has the smallest sum of squared deviations from the experimental points.

Analyzing the experimental data, it is necessary to note that there was a background concentration of capsules in the intact lung. Moreover, the background concentration was higher for micron capsules than for submicron ones: $(6.6 \pm 3.1)\%$ and $(4.9 \pm 2.8)\%$, respectively. The number of capsules that actually accumulated in the lung under the influence of the magnetic field was significantly lower than those that reached the capillary wall. As Figure 10 shows, the calculated percentage of capsules that reach the capillary wall is not more than 80% for submicron capsules and 67% for micron ones. The experimentally measured values for these levels are 51% and 28%, respectively. Significant differences in concentrations between the left lung (influenced by the magnet) and the right one (intact)

were observed till the distances of 13.5 mm and 10.5 mm from the magnet for submicron and micron capsules, respectively.

The parameters of function (24), describing the probability of the capsule being retained near the wall, are as follows: $f_0 = 1220$ m/s^2 and $\Delta f = 540$ m/s^2 for submicron capsules, and $f_0 = 1590$ m/s^2 and $\Delta f = 690$ m/s^2 for micron ones. As can be seen, the parameter f_0, which characterizes the specific magnetic force required to keep the capsules near the capillary wall, is 1.3 times greater for micron-sized capsules compared to submicron-sized ones. This is likely due to the fact that larger capsules experience a greater drag force from fluid flow and have a higher probability of collision with blood cells in the bloodstream. It is worth noting that the in vivo and in vitro experimental results are consistent: in both cases, the number of deposited capsules was lower than the theoretically calculated number of capsules reaching the capillary wall under the influence of the magnetic field. In both cases, the introduction of a deposition probability function containing only two fitting parameters allowed for a satisfactory approximation of the experimental curves for all measured points.

4. Discussion

4.1. Estimation of Magnetic Field Parameters

The development of a new drug delivery system requires significant effort and material investment. In this regard, it is practically important to have a tool that allows one to estimate the capabilities of the proposed scheme prior to its experimental implementation. In particular, it is important to have an easy-to-use criterion for assessing the magnetic field characteristics. The concept of specific magnetic force, introduced in this study, provides a convenient parameter for this purpose. As the calculations show, the magnetic field has the most significant effect on the capsules when the magnetic force acts perpendicular to the flow. In a straight cylindrical capillary placed in a magnetic field perpendicular to it, it is possible to estimate the minimum specific magnetic force required for delivery of all capsules to the capillary wall closest to the magnet. For this, a capsule must have enough time to move from the farthest capillary wall to the wall closest to the magnet.

The time $t_{\parallel}$ of the capsule's longitudinal motion is determined by the averaged velocity $\langle v \rangle$ of the liquid flow and the length l of the capillary:

$$t_{\parallel} = \frac{l}{\langle v \rangle} . \tag{27}$$

The velocity $\langle v \rangle$ is averaged along the capillary diameter and is equal to $4/3\overline{v}$, where $\overline{v}$ is the flux averaged velocity. The time $t_{\perp}$ of perpendicular motion is determined by magnetic force f_m, which makes the particles move relative to the liquid with the stationary speed v_r:

$$t_{\perp} = \frac{2R}{v_r}, \tag{28}$$

where R is the capillary radius. From Equation (15), we can obtain $v_r = \frac{m_{mag}}{6\pi\eta r} f_m$ and then we obtain

$$t_{\perp} = \frac{12R\pi r\eta}{m_{mag} f_m}. \tag{29}$$

The necessary condition of precipitation of all capsules in magnetic field is $t_{\perp} < t_{\parallel}$. From this inequality, we obtain the effective value of f_m necessary for magnetic driven delivery:

$$f_m^{eff} = 16\pi \frac{R}{l} \frac{r\eta\overline{v}}{m_{mag}} . \tag{30}$$

One can see that Equation (30) contains parameters of the blood flow in the capillary (R, l, $\overline{v}$, and η) and of the microcapsule (r and m_{mag}). The first group of parameters lies outside the researcher's influence, while the parameters r and m_{mag} can be controlled. It is worth noting that the properties of the magnetic capsule are determined by the ratio (m_{mag}/r). In the case of constant concentration of the magnetic substance, this parameter increases proportionally to r^2 with increasing capsule size.

Using Equation (30) and the parameters of the blood capillary given in Section 3.4, we obtained the values of effective f_m for both types of the capsules: $f_m^{eff} = 1980$ m/s^2 for submicron capsules and $f_m^{eff} = 2620$ m/s^2 for micron capsules, respectively.

4.2. Estimation of Maximal Distance from the Magnet to the Target

The parameter f_m^{eff} helps us to determine the maximal distance from the magnet to the area in which the capsules are effectively controlled by a magnetic field. It should be noted that obtaining high values of magnetic force in the immediate vicinity of the surface of a magnet is not a very difficult problem, as large values of f_m can be achieved through the use of high field gradients. For instance, such fields can be found in high-gradient magnetic separation systems [45]. However, in such fields, f_m decreases rapidly with distance. If the aim is to achieve a strong enough field for effective targeted drug delivery at the largest possible distance from the magnet, other configurations should be considered.

Let us consider the most common and useful cylindrical shape of a magnet with the target located at the axis of the cylinder. It is worth noting that at short distances from the cylindrical magnet, the specific magnetic force f_m will be greater near the edges of the base compared to the center due to the larger gradient [42]. However, the field strength near the edges decreases more rapidly with distance, so if the goal is to achieve f_m^{eff} at the greatest given distance from the magnet, an axial target position may be preferable. Let us first consider the behavior of magnetic force on the axis of the magnet, which allows for an explicit analytical solution, and then proceed with a numerical analysis that includes the field near the edges.

The magnetic field on the axis of the cylinder of radius R_m and height h is given by the following:

$$B_z = B_0 \left(\frac{z+h}{\sqrt{R_m^2 + (z+h)^2}} - \frac{z}{\sqrt{R_m^2 + z^2}} \right), \tag{31}$$

where z is the distance from the base of the cylinder and B_0 is the field on the center of the base. It is clear from Equation (31) that the magnetic field increases with the increase in cylinder height. In the case of a long cylinder ($h \gg R_m$ and $h \gg z$), the formula for the magnetic field takes the following form:

$$B_z = B_0 \left(1 - \frac{z}{\sqrt{R_m^2 + z^2}} \right). \tag{32}$$

To determine the specific magnetic force f_m, we need the value of the field gradient:

$$\frac{\partial B_z}{\partial z} = -B_0 \frac{R_m^2}{(R_m^2 + z^2)^{\frac{3}{2}}}. \tag{33}$$

Using the Equation (11) and approximation (22) for the magnetic moment of the capsule, we obtain the following equation for the absolute value of f_m:

$$f_m = \sigma_s B_0 L \left(\frac{B(z)}{B_c} \right) \frac{R_m^2}{(R_m^2 + z^2)^{\frac{3}{2}}}. \tag{34}$$

Now, substituting f_m^{eff} into the left-hand side of Equation (34), we obtain the equation for the radius of magnet R_m and the distance z at which the specific magnetic force f_m reaches the value f_m^{eff}:

$$f_m^{eff} = \sigma_s B_0 L\left(\frac{B_0}{B_c}\left(1 - \frac{z}{\left(R_m^2 + z^2\right)^{\frac{1}{2}}}\right)\right)\frac{R_m^2}{\left(R_m^2 + z^2\right)^{\frac{3}{2}}}. \tag{35}$$

Let us reduce the equation to the dimensionless variables. For this reason, we introduce the characteristic magnet radius R_c by the following formula:

$$R_c = \frac{\sigma_s B_0 L\left(\frac{B_0}{B_c}\right)}{f_m^{eff}}. \tag{36}$$

One can see that Equation (35) is satisfied at $z = 0$ if the radius of the magnet equals R_c. This parameter is a useful unit of length for the considered problem. Now let us introduce the dimensionless variables $\rho = R_m/R_c$, and $\zeta = z/R_c$. Then, Equation (35) takes the following form:

$$L\left(\frac{B_0}{B_c}\right) = L\left(\frac{B_0}{B_c}\left(1 - \frac{\zeta}{\left(\rho^2 + \zeta^2\right)^{\frac{1}{2}}}\right)\right)\frac{\rho^2}{\left(\rho^2 + \zeta^2\right)^{\frac{3}{2}}}. \tag{37}$$

This equation contains only one parameter, B_0/B_c, which can take any value from zero to infinity. All possible variants of magnetization behavior lie between these two extreme cases. The limit of $B_0 \gg B_c$ corresponds to constant specific magnetization $\sigma = const$ as long as Langerin's function L in Equation (22) is equal to unity. The value of R_c in this case takes the following form:

$$R_c = \sigma_s \frac{B_0}{f_m^{eff}} \tag{38}$$

and Equation (37) is significantly simplified:

$$\frac{\rho^2}{\left(\rho^2 + \zeta^2\right)^{\frac{3}{2}}} = 1. \tag{39}$$

This equation has an exact solution:

$$\zeta(\rho) = \rho^{\frac{2}{3}}\left(1 - \rho^{\frac{2}{3}}\right)^{\frac{1}{2}}. \tag{40}$$

It is easy to show that the function $\zeta(\rho)$ reaches its maximal value $\zeta_{max} = 0.39$ at $\rho_m = 0.55$.

Another important case is $B_0 \ll B_c$ when the Langevin function becomes linear and specific magnetization can be described in terms of constant magnetic susceptibility $\chi = \sigma_s/(3B_c)$. The characteristic radius in this case is given by $R_c = \chi B_0^2/f_m^{eff}$. Equation (37) is simplified too and takes the following form:

$$\left(1 - \frac{\zeta}{\left(\rho^2 + \zeta^2\right)^{\frac{1}{2}}}\right)\frac{\rho^2}{\left(\rho^2 + \zeta^2\right)^{\frac{3}{2}}} = 1. \tag{41}$$

We solved this numerically with Scilab 6.1.1. The obtained values of maximal ζ_{max} and corresponding ρ_m are equal to 0.20 and 0.48, respectively.

For submicron particles and the magnet used in our experiments, the parameter B_0/B_c equals to 24. To find the dependence $\zeta(\rho)$ in this case, we solved Equation (37) numerically and from the analysis of the curve obtained $\zeta_{max} = 0.37$ and $\rho_m = 0.55$.

The dependencies $z_m = R_c\zeta(\rho)$ for different values of parameter B_c/B_0 are shown in Figure 11. One can see that with increase in the magnet radius R_m the distance z_m at which f_m reaches the value f_m^{eff} initially increases and then goes down to zero. The value of magnet radius R_m, for which this distance is maximal, equals approximately half of R_c. The value z_{max} of maximal distance lies in the range from 0.20 R_c to 0.39 R_c.

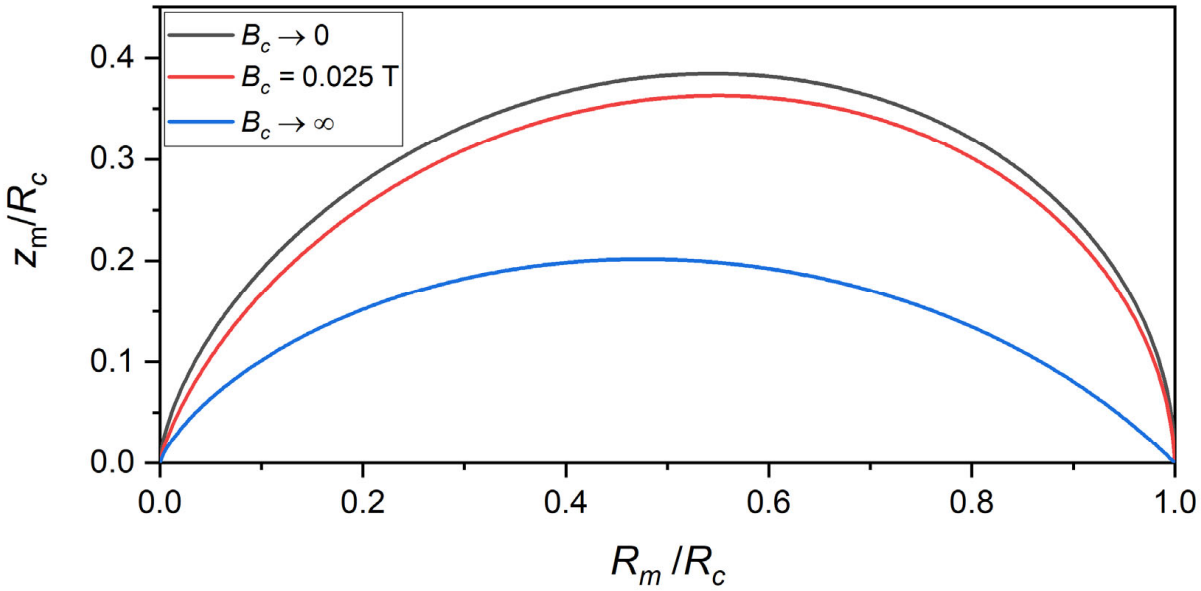


Figure 11. The maximal distance z_m at which the value f_m^{eff} can be achieved as a function of the magnet radius R_m. Both values are given in units of characteristic magnet radius R_c defined by Equation (36). Colors represent different types of magnetization curve: the black line corresponds to $B_c \to 0$ (saturation in weak fields), the blue line corresponds to $B_c \to \infty$ (linear dependence of magnetization on the field), and the red line corresponds to $B_c = 0.025\ T$, which is observed in the case of submicron capsules.

Let us now examine whether it is possible to achieve greater values of z near the edges of the magnet. To do this, we investigated numerically with Scilab 6.1.1 the line of constant level for f_m in the plane passing through the magnet's axis as a function $z(x)$. We determined its maximum within the interval $x \in [-1.2R_m, 1.2R_m]$ and studied how this maximum depends on the radius R_m of the magnet. As Figure 2 shows, the constant-level line for f_m may have a single maximum, as in the case of $f_m = 1000$ m/s^2, or two maxima, as in the case of $f_m = 2000$ m/s^2. The single maximum is located on the magnet axis. The dependence of the maximum distance z_m, at which the required value of f_m is achieved on the magnet radius, is shown in Figure 12. The dashed lines represent the values of z_m on the magnet axis obtained analytically.

It can be seen from Figure 12 that for small radii, the solid and dashed lines coincide, since the maximum of z_m is reached on the magnet's axis in this case. Starting from $R_m = 1.25$ cm for submicron capsules and from $R_m = 0.9$ cm for micron-sized ones, the solid lines rise above the dashed line. After reaching its maximum, the dashed line drops to zero, whereas the solid line increases slightly and then gradually decreases as well. Although the maximum of the solid lines is slightly higher than that of the dashed ones, our calculations show that the difference does not exceed 0.03 mm. With further increase in the magnet's size, the region where the magnetic force exceeds the specified value takes on a shape close to that of a torus. In our opinion, achieving the desired field on the axis

seems to be more practical, since in this case, the region of the field exceeding the critical value has a smaller width at the same depth compared to the field near the edge of a larger magnet.

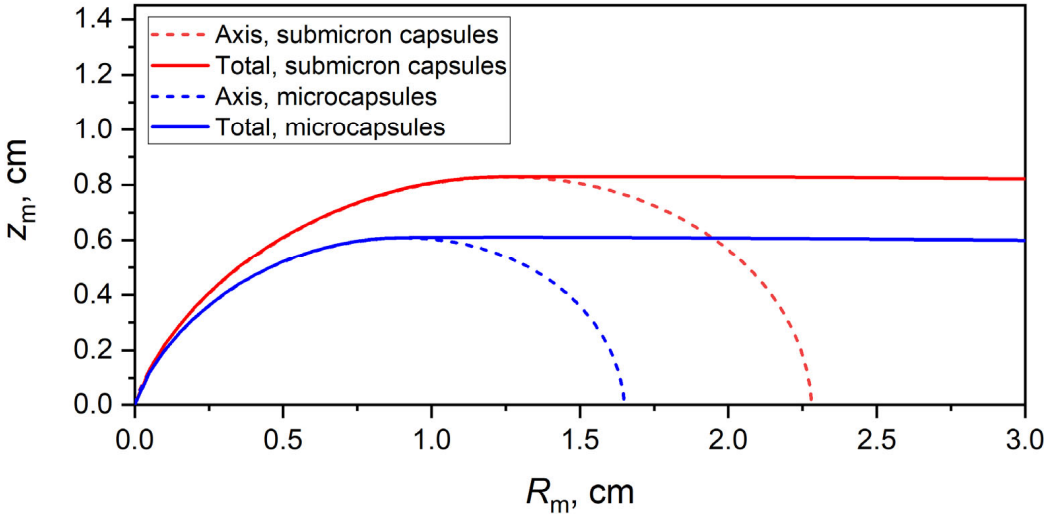


Figure 12. The maximum distance z_m, at which the value f_m^{eff} is achieved, as a function of the radius of the magnet. The height of the magnet is taken to be infinite. The red lines correspond to $f_m^{eff} = 1980$ m/s^2 for submicron capsules, and the blue lines correspond to $f_m^{eff} = 2620$ m/s^2 for microcapsules. The dashed lines represent z_m on the axis, while the solid lines represent z_m calculated over the entire base of the magnet.

Table 1 shows the calculated values of parameter f_m^{eff} for a few types of magnetic capsules (synthesized in our group and other scientific teams [21,36]). The values of f_m^{eff} were obtained using Equation (30), and the same parameters of blood vessels were taken for calculations in Section 3.4. The table also shows the radius R_m of a long cylindrical NdFeB magnet, which allows one to achieve the required values of magnetic force at the maximum distance from the surface. The last column represents the distance z_{max} at which such a field can be achievable. The values of R_m and z_{max} were calculated using Equation (36) and values of ρ_m and ζ_{max}. All types of capsules shown in the table contain iron oxide nanoparticles having similar physical and chemical characteristics.

Table 1. Calculated values of effective specific magnetic force and magnet dimensions required for the precipitation of various polymer capsules in capillaries.

Capsule Radius, μm	Mass of Fe_3O_4 Per Capsule, pg	m_{mag}/r, pg/μm	f_m^{eff}, m/s^2	Optimal Diameter of the Magnet, cm	Distance from the Magnet, cm	Ref.
1.25	1.5	1.20	2620	1.81	0.61	
0.41	0.65	1.59	1980	2.50	0.84	
2.1	5.7	2.71	1160	4.10	1.37	[36]
0.25	0.29	1.16	2710	1.83	0.61	[21]

Table 1 allows us to estimate the distance from the magnet at which the capsule precipitation is possible and to select the necessary parameters of the capsules and magnet to perform magnetic targeted drug delivery with necessary depth. It should be mentioned that in all cases, the distance at which f_m^{eff} is achieved is approximately three times less than the diameter of the magnet.

Using more powerful sources of a magnetic field, for example, superconducting or actively cooled electromagnets, it is possible to obtain the required values of f_m at a greater depth from the body surface. However, in practice, it is technically difficult to achieve magnetic field strengths and gradients greater than those produced by high-performance permanent magnets. It also needs to be kept in mind that regardless of the type of the source of magnetic field, all tissues located closer to the body surface are also in the zone of higher magnetic force.

It is important to note that magnetic force sufficient for sedimentation of the capsules will be achieved not only at one specific point, but in a fairly large area with a shape similar to a mushroom cap as represented in Figure 2. It was shown in the work [34] for the two-dimensional case that for any configuration of external sources of a static magnetic field, it is impossible to achieve a maximum of the magnetic force inside a living organism (we did not find the proof of this statement for the three-dimensional case, but we also do not know examples of fields that violate this statement). Therefore, it is impossible to produce a targeted drag delivery into some internal point of the body without affecting the area located close to the body surface.

4.3. Limitations of Our Work

The theoretical approaches used in the work have certain limitations. Theoretical calculations for the in vivo experiment were performed using a model of a straight cylindrical capillary. The liquid velocity profile was assumed to follow Poiseuille's theory. The curvature of capillaries and disturbing of fluid velocities by the blood cells was not taken into account. Therefore, the values of the parameter f_m^{eff} obtained within this model should be considered as approximate to a certain extent. The analytical evaluation of the distances at which f_m^{eff} is achieved were carried out only for the magnetic field at the axis of a cylindrical longitudinally magnetized magnet. Therefore, new calculations are needed when using magnets of a different shape or with a different spatial orientation.

5. Conclusions

Targeted drug delivery using magnetic particles is still the "golden dream" of biomedical researchers. Indeed, it looks very elegant and safe: magnets can be placed outside the body surface, and they do not have a harmful effect on human organs and tissues. However, it should be noted that a clinically applicable system for magnetically controlled delivery has not yet been developed.

In this paper, we attempted to create an approach that would theoretically predict the possibility of magnetic targeting in a living organism based on carriers' parameters and field characteristics. To solve the problem, we developed a theory for the motion of magnetic microcapsules in a fluid flow in the presence of a non-uniform magnetic field. Using this theory, we estimated the parameters of both the magnetic field and the capsules required to deposit them in a specific area of the organism. Based on the developed theory, we proposed a convenient parameter to estimate the field—"specific magnetic force"—which is equal to the ratio of magnetic force to the mass of magnetic material in the capsule. We derived a formula for the minimum value of this parameter at which all capsules in the flow will reach the capillary wall.

Experiments were conducted both in vitro (using plastic models of capillaries) and in vivo (on mini pigs) in order to determine the actual number of capsules that are deposited in a magnetic field. An approximation function was proposed for the relationship between the probability of capsule deposition and the value of magnetic force. Using this function, we were able to derive a theoretical distribution for the number of deposited capsules, which was in good agreement with our experimental results. We also calculated the

maximum distance at which magnetically controlled capsule deposition can be achieved using a cylindrical permanent NdFeB magnet.

Thus, the conducted study allows us to systematically organize data on the factors influencing the behavior of magnetic particles in the capillaries of living organisms and to predict the possibility for magnetic targeting. This brings us closer to the creation of effective systems for magnetic drug delivery for the treatment of currently important diseases.

Supplementary Materials: The following supporting information can be downloaded at: https://www.mdpi.com/article/10.3390/magnetochemistry11070060/s1; Figure S1. Calibration curve for quantitative analysis of DOX in aqueous solutions; Figure S2. Calibration curve for quantitative analysis of DOX in blood; Figure S3. Calibration curve for quantitative analysis of DOX in lung tissue.

Author Contributions: Conceptualization, M.N.Z., M.A.P., G.B.S. and N.A.P.; data curation, M.A.P., D.E.Y., V.P.A., O.A.K. and V.I.S.; formal analysis, M.N.Z., M.A.P., D.E.Y., V.P.A., O.A.K. and L.A.B.; investigation, M.N.Z., M.A.P., D.E.Y., V.I.S., D.N.K. and N.A.P.; methodology, M.N.Z., M.A.P., O.A.K., L.A.B., G.B.S. and N.A.P.; visualization, D.N.K.; writing—original draft, M.N.Z., M.A.P., G.B.S. and N.A.P.; writing—review and editing, N.A.P. All authors have read and agreed to the published version of the manuscript.

Funding: In part of electron microscopy this work was performed within State assignment for NRC "Kurchatov Institute" using the equipment of Shared Research Center "Structural Diagnostics of Materials" of the Kurchatov Complex Crystallography and Photonics.

Institutional Review Board Statement: The animal study protocol was approved by the local ethics committee of the Medical Institute of National Research Mordovia State University, approval date: 15 September 2023, approval code: 119.

Data Availability Statement: Primary data are stored at the research center (MRSU) and can be accessed upon request from any of the corresponding authors.

Conflicts of Interest: The authors declare that they have no known competing financial interests or personal relationships that could appear to influence the work reported in this paper.

Abbreviations

The following abbreviations are used in this manuscript:

DOX	doxorubicin
TEM	transmission electron microscopy
PAH	polyallylamine hydrochloride
DexS	dextran sulfate
PSS	polystyrene sulfonate sodium
PBS	phosphate buffered saline

References

1. Jose, G.; Lu, Y.-J.; Chen, H.-A.; Hsu, H.-L.; Hung, J.-T.; Anilkumar, T.S.; Chen, J.-P. Hyaluronic Acid Modified Bubble-Generating Magnetic Liposomes for Targeted Delivery of Doxorubicin. *J. Magn. Magn. Mater.* **2019**, *474*, 355–364. [CrossRef]
2. Lu, Y.-J.; Chuang, E.-Y.; Cheng, Y.-H.; Anilkumar, T.S.; Chen, H.-A.; Chen, J.-P. Thermosensitive Magnetic Liposomes for Alternating Magnetic Field-Inducible Drug Delivery in Dual Targeted Brain Tumor Chemotherapy. *Chem. Eng. J.* **2019**, *373*, 720–733. [CrossRef]
3. Huang, C.; Tang, Z.; Zhou, Y.; Zhou, X.; Jin, Y.; Li, D.; Yang, Y.; Zhou, S. Magnetic Micelles as a Potential Platform for Dual Targeted Drug Delivery in Cancer Therapy. *Int. J. Pharm.* **2012**, *429*, 113–122. [CrossRef] [PubMed]
4. Paul, W.; Sharma, C.P. Inorganic Nanoparticles for Targeted Drug Delivery. In *Biointegration of Medical Implant Materials*; Elsevier: Amsterdam, The Netherlands, 2020; pp. 333–373. ISBN 978-0-08-102680-9.
5. Ashi, M.; Indrajit, R.; Sona, G. Magnetic Nanoparticles: An Overview for Biomedical Applications. *Magnetochemestry* **2022**, *8*, 107. [CrossRef]

6. Shabatina, T.I.; Vernaya, O.I.; Shabatin, V.P.; Melnikov, M.Y. Magnetic Nanoparticles for Biomedical Purposes: Modern Trends and Prospects. *Magnetochemestry* **2020**, *6*, 30. [CrossRef]
7. Podgórna, K.; Szczepanowicz, K. Synthesis of Polyelectrolyte Nanocapsules with Iron Oxide (Fe_3O_4) Nanoparticles for Magnetic Targeting. *Colloids Surf. Physicochem. Eng. Asp.* **2016**, *505*, 132–137. [CrossRef]
8. Attari, E.; Nosrati, H.; Danafar, H.; Kheiri Manjili, H. Methotrexate Anticancer Drug Delivery to Breast Cancer Cell Lines by Iron Oxide Magnetic Based Nanocarrier. *J. Biomed. Mater. Res. A* **2019**, *107*, 2492–2500. [CrossRef]
9. Lotfipour, F.; Azhar Shekoufeh, L.B. Magnetic Nanoparticles for Antimicrobial Drug Delivery. *Pharmazie* **2012**, *67*, 817–821. [CrossRef]
10. Du, X.; Chen, K.; Kuriyavar, S.; Kopke, R.D.; Grady, B.P.; Bourne, D.H.; Li, W.; Dormer, K.J. Magnetic Targeted Delivery of Dexamethasone Acetate Across the Round Window Membrane in Guinea Pigs. *Otol. Neurotol.* **2013**, *34*, 41–47. [CrossRef]
11. McBain, S.; Yiu, H.; Dobson, J. Magnetic Nanoparticles for Gene and Drug Delivery. *Int. J. Nanomed.* **2008**, *3*, 169–180. [CrossRef]
12. Solaro, R.; Chiellini, F.; Battisti, A. Targeted Delivery of Protein Drugs by Nanocarriers. *Materials* **2010**, *3*, 1928–1980. [CrossRef]
13. Koudan, E.V.; Zharkov, M.N.; Gerasimov, M.V.; Karshieva, S.S.; Shirshova, A.D.; Chrishtop, V.V.; Kasyanov, V.A.; Levin, A.A.; Parfenov, V.A.; Karalkin, P.A.; et al. Magnetic Patterning of Tissue Spheroids Using Polymer Microcapsules Containing Iron Oxide Nanoparticles. *ACS Biomater. Sci. Eng.* **2021**, *7*, 5206–5214. [CrossRef] [PubMed]
14. Verkhovskii, R.; Ermakov, A.; Grishin, O.; Makarkin, M.A.; Kozhevnikov, I.; Makhortov, M.; Kozlova, A.; Salem, S.; Tuchin, V.; Bratashov, D. The Influence of Magnetic Composite Capsule Structure and Size on Their Trapping Efficiency in the Flow. *Molecules* **2022**, *27*, 6073. [CrossRef]
15. Blümler, P.; Friedrich, R.P.; Pereira, J.; Baun, O.; Alexiou, C.; Mailänder, V. Contactless Nanoparticle-Based Guiding of Cells by Controllable Magnetic Fields. *Nanotechnol. Sci. Appl.* **2021**, *14*, 91–100. [CrossRef]
16. Nacev, A.; Komaee, A.; Sarwar, A.; Probst, R.; Kim, S.H.; Emmert-Buck, M.; Shapiro, B. Towards Control of Magnetic Fluids in Patients: Directing Therapeutic Nanoparticles to Disease Locations. *IEEE Control. Syst.* **2012**, *32*, 32–74. [CrossRef]
17. Baun, O.; Blümler, P. Permanent magnet system to guide superparamagnetic particles. *J. Magn. Magn. Mater.* **2017**, *439*, 294–304. [CrossRef]
18. Blümler, P. Magnetic Guiding with Permanent Magnets: Concept, Realization and Applications to Nanoparticles and Cells. *Cells* **2021**, *10*, 2708. [CrossRef]
19. Rivière, C.; Martina, M.-S.; Tomita, Y.; Wilhelm, C.; Tran Dinh, A.; Ménager, C.; Pinard, E.; Lesieur, S.; Gazeau, F.; Seylaz, J. Magnetic Targeting of Nanometric Magnetic Fluid–Loaded Liposomes to Specific Brain Intravascular Areas: A Dynamic Imaging Study in Mice. *Radiology* **2007**, *244*, 439–448. [CrossRef]
20. Svenskaya, Y.; Garello, F.; Lengert, E.; Kozlova, A.; Verkhovskii, R.; Bitonto, V.; Ruggiero, M.R.; German, S.; Gorin, D.; Terreno, E. Biodegradable Polyelectrolyte/Magnetite Capsules for MR Imaging and Magnetic Targeting of Tumors. *Nanotheranostics* **2021**, *5*, 362–377. [CrossRef]
21. Novoselova, M.V.; German, S.V.; Sindeeva, O.A.; Kulikov, O.A.; Minaeva, O.V.; Brodovskaya, E.P.; Ageev, V.P.; Zharkov, M.N.; Pyataev, N.A.; Sukhorukov, G.B.; et al. Submicron-Sized Nanocomposite Magnetic-Sensitive Carriers: Controllable Organ Distribution and Biological Effects. *Polymers* **2019**, *11*, 1082. [CrossRef]
22. Janikowska, A.; Matuszak, J.; Lyer, S.; Schreiber, E.; Unterweger, H.; Zaloga, J.; Groll, J.; Alexiou, C.; Cicha, I. A Novel Human Artery Model to Assess the Magnetic Accumulation of SPIONs under Flow Conditions. *Sci. Rep.* **2017**, *7*, 42314. [CrossRef] [PubMed]
23. Kulkarni, S.; Ramaswamy, B.; Horton, E.; Gangapuram, S.; Nacev, A.; Depireux, D.; Shimoji, M.; Shapiro, B. Quantifying the Motion of Magnetic Particles in Excised Tissue: Effect of Particle Properties and Applied Magnetic Field. *J. Magn. Magn. Mater.* **2015**, *393*, 243–252. [CrossRef]
24. Alexiou, C.; Jurgons, R.; Schmid, R.; Hilpert, A.; Bergemann, C.; Parak, F.; Iro, H. In Vitro and in Vivo Investigations of Targeted Chemotherapy with Magnetic Nanoparticles. *J. Magn. Magn. Mater.* **2005**, *293*, 389–393. [CrossRef]
25. Chen, H.; Kaminski, M.D.; Pytel, P.; Macdonald, L.; Rosengart, A.J. Capture of Magnetic Carriers within Large Arteries Using External Magnetic Fields. *J. Drug Target.* **2008**, *16*, 262–268. [CrossRef] [PubMed]
26. Lübbe, A.S.; Bergemann, C.; Riess, H.; Schriever, F.; Reichardt, P.; Possinger, K.; Matthias, M.; Dörken, B.; Herrmann, F.; Gürtler, R.; et al. Clinical Experiences with Magnetic Drug Targeting: A Phase I Study with 4′-Epidoxorubicin in 14 Patients with Advanced Solid Tumors. *Cancer Res.* **1996**, *56*, 4686–4693.
27. Sharma, S.; Ram, P. Capturing of Magnetic Nanoparticles in a Fluidic Channel for Magnetic Drug Targeting. *J. Nanosci. Nanotechnol.* **2021**, *21*, 3588–3595. [CrossRef]
28. Nacev, A.; Beni, C.; Bruno, O.; Shapiro, B. The Behaviors of Ferromagnetic Nano-Particles in and around Blood Vessels under Applied Magnetic Fields. *J. Magn. Magn. Mater.* **2011**, *323*, 651–668. [CrossRef]
29. Heidsieck, A.; Vosen, S.; Zimmermann, K.; Wenzel, D.; Gleich, B. Analysis of Trajectories for Targeting of Magnetic Nanoparticles in Blood Vessels. *Mol. Pharm.* **2012**, *9*, 2029–2038. [CrossRef]

30. Sharma, S.; Katiyar, V.K.; Singh, U. Mathematical modelling for trajectories of magnetic nanoparticles in a blood vessel under magnetic field. *J. Magn. Magn. Mater.* **2015**, *379*, 102–107. [CrossRef]
31. David, A.E.; Cole, A.J.; Chertok, B.; Park, Y.S.; Yang, V.C. A combined theoretical and in vitro modeling approach for predicting the magnetic capture and retention of magnetic nanoparticles in vivo. *J. Control. Release* **2011**, *152*, 67–75. [CrossRef]
32. Furlani, E.J.; Furlani, E.P. A Model for Predicting Magnetic Targeting of Multifunctional Particles in the Microvasculature. *J. Magn. Magn. Mater.* **2007**, *312*, 187–193. [CrossRef]
33. Shaw, S.; Murthy, P.V.S.N.; Pradhan, S.C. Effect of Non-Newtonian Characteristics of Blood on Magnetic Targeting in the Impermeable Micro-Vessel. *J. Magn. Magn. Mater.* **2010**, *322*, 1037–1043. [CrossRef]
34. Grief, A.D.; Richardson, G. Mathematical Modelling of Magnetically Targeted Drug Delivery. *J. Magn. Magn. Mater.* **2005**, *293*, 455–463. [CrossRef]
35. Sharifi, A.; Motlagh, S.Y.; Badfar, H. Numerical Investigation of Magnetic Drug Targeting Using Magnetic Nanoparticles to the Aneurysmal Vessel. *J. Magn. Magn. Mater.* **2019**, *474*, 236–245. [CrossRef]
36. Zharkov, M.N.; Brodovskaya, E.P.; Kulikov, O.A.; Gromova, E.V.; Ageev, V.P.; Atanova, A.V.; Kozyreva, Z.V.; Tishin, A.M.; Pyatakov, A.P.; Pyataev, N.A.; et al. Enhanced Cytotoxicity Caused by AC Magnetic Field for Polymer Microcapsules Containing Packed Magnetic Nanoparticles. *Colloids Surf. B Biointerfaces* **2021**, *199*, 111548. [CrossRef] [PubMed]
37. Shushunova, N.A.; Mayorova, O.A.; Prikhozhdenko, E.S.; Goryacheva, O.A.; Kulikov, O.A.; Plastun, V.O.; Gusliakova, O.I.; Muslimov, A.R.; Inozemtseva, O.A.; Pyataev, N.A.; et al. Targeted Therapy for Glomerulonephritis Using Arterial Delivery of Encapsulated Etanercept. *Int. J. Mol. Sci.* **2023**, *24*, 2784. [CrossRef]
38. Pozdnyakov, I.P.; Plyusnin, V.F.; Grivin, V.P.; Vorobyev, D.Y.; Bazhin, N.M.; Pagés, S.; Vauthey, E. Photochemistry of Fe(III) and Sulfosalicylic Acid Aqueous Solutions. *J. Photochem. Photobiol. Chem.* **2006**, *182*, 75–81. [CrossRef]
39. Laginha, K.M.; Verwoert, S.; Charrois, G.J.R.; Allen, T.M. Determination of Doxorubicin Levels in Whole Tumor and Tumor Nuclei in Murine Breast Cancer Tumors. *Clin. Cancer Res.* **2005**, *11*, 6944–6949. [CrossRef]
40. Laura Soriano, M.; Carrillo-Carrion, C.; Ruiz-Palomero, C.; Valcárcel, M. Cyclodextrin-Modified Nanodiamond for the Sensitive Fluorometric Determination of Doxorubicin in Urine Based on Its Differential Affinity towards β/γ-Cyclodextrins. *Microchim. Acta* **2018**, *185*, 115. [CrossRef]
41. Furlani, E.P. *Permanent Magnet and Electromechanical Devices: Materials, Analysis, and Applications*; Academic Press: Cambridge, MA, USA, 2021.
42. Zablotskii, V.; Polyakova, T.; Lunov, O.; Dejneka, A. How a High-Gradient Magnetic Field Could Affect Cell Life. *Sci. Rep.* **2016**, *6*, 37407. [CrossRef]
43. Gruber, S.; Spielauer, I.; Böhme, S.; Baron, D.; Markstaller, K.; Ullrich, R.; Klein, K.U. Real-time in-vivo imaging of pulmonary capillary perfusion using probe-based confocal laser scanning endomicroscopy in pigs. *Eur. J. Anaesthesiol.* **2015**, *32*, 392–399. [CrossRef] [PubMed]
44. Windberger, U.; Bartholovitsch, A.; Plasenzotti, R.; Korak, K.J.; Heinze, G. Whole Blood Viscosity, Plasma Viscosity and Erythrocyte Aggregation in Nine Mammalian Species: Reference Values and Comparison of Data. *Exp. Physiol.* **2003**, *88*, 431–440. [CrossRef] [PubMed]
45. Ge, W.; Encinas, A.; Araujo, E.; Song, S. Magnetic Matrices Used in High Gradient Magnetic Separation (HGMS): A Review. *Results Phys.* **2017**, *7*, 4278–4286. [CrossRef]

Disclaimer/Publisher's Note: The statements, opinions and data contained in all publications are solely those of the individual author(s) and contributor(s) and not of MDPI and/or the editor(s). MDPI and/or the editor(s) disclaim responsibility for any injury to people or property resulting from any ideas, methods, instructions or products referred to in the content.